

Magnetic phases and electron-phonon coupling in $\text{La}_3\text{Ni}_2\text{O}_7$ under pressure

Cong Zhu^a, Bin Li^{b,c,*}, Yuxiang Fan^b, Chuanhui Yin^a, Junjie Zhai^{b,d}, Jie Cheng^{b,c}, Shengli Liu^{b,c,*}, Zhixiang Shi^e

^a*College of Electronic and Optical Engineering Nanjing University of Posts and Telecommunications Nanjing 210023 China*

^b*School of Science Nanjing University of Posts and Telecommunications Nanjing 210023 China*

^c*Jiangsu Provincial Engineering Research Center of Low Dimensional Physics and New Energy Nanjing University of Posts and Telecommunications Nanjing 210023 China*

^d*University of Chinese Academy of Sciences Nanjing (UCASNJ) Nanjing 211135 China*

^e*School of Physics Southeast University Nanjing 211189 China*

Abstract

Motivated by recent reports of pressure-induced superconductivity in bilayer nickelate $\text{La}_3\text{Ni}_2\text{O}_7$, we present a comprehensive investigation into the structural, electronic, magnetic, and phonon properties of this compound across a pressure range of 0 to 29.5 GPa. DFT+U calculations reveal that the A-type antiferromagnetic ground state of $\text{La}_3\text{Ni}_2\text{O}_7$ persists throughout the studied pressure range. Electronic structure analysis shows that the Ni- d_{xy} and Ni- d_{z^2} orbitals dominate near the Fermi level in both the $Fmmm$ and $Amam$ phases of $\text{La}_3\text{Ni}_2\text{O}_7$. Phonon dispersion calculations for the $Fmmm$ phase reveal no imaginary modes from 12 to 29.5 GPa, confirming its dynamical stability in this pressure range. The vibrational frequencies of O atoms are substantially higher than those of Ni and La atoms, primarily due to the lower mass of oxygen. At 29.5 GPa, the electron-phonon coupling constant λ for the $Fmmm$ phase is calculated to be 0.13. This small value suggests that conventional electron-phonon coupling is insufficient to explain the reported superconductivity in $\text{La}_3\text{Ni}_2\text{O}_7$, indicating a potentially unconventional mechanism. The study offers nuanced, actionable insights that can strategically inform and direct subsequent experimental investigations into

*Corresponding author.

Email addresses: libin@njupt.edu.cn (Bin Li), liusl@njupt.edu.cn (Shengli Liu)

the design and optimization of nickel-based superconducting materials.

Keywords: superconductivity, first-principles calculation, bilayer nickelate $\text{La}_3\text{Ni}_2\text{O}_7$, band structure, magnetic configurations, electron-phonon coupling

1. Introduction

The observation of superconductivity in low valence layered nickelates has generated immense excitement in the community over the past few years[1, 2, 3]. Recently, the newly discovered Ruddlesden-Popper bilayer perovskite nickelate $\text{La}_3\text{Ni}_2\text{O}_7$ has demonstrated a remarkable high superconducting transition temperature of $T_c \sim 80$ K at an applied pressure exceeding 14 GPa[4, 5, 6]. This breakthrough is poised to create a significant impact in the field of high- T_c superconductivity, long after the discoveries of cuprate and iron-based superconductors. Given the identical $3d$ electronic configuration of Ni^{1+} in the parent phase, which is isoelectronic with Cu^{2+} , and the presence of comparable NiO_2 or CuO_2 layers, it was anticipated that the superconducting mechanism of the interlayer (IL) nickelate would closely mimic that of the cuprates. In the cuprates, superconductivity emerged upon hole doping, leading to expectations that a similar phenomenon could be observed in the IL nickelate as well[7]. However, numerous theoretical and experimental investigations have revealed fundamental differences between the individual infinite-layer nickelate and the cuprates[8, 9, 10, 11, 12].

The discovery of a high-temperature superconducting nickel oxide with a $\text{Ni}^{2.5+}$ valence state has been groundbreaking, as its electronic structure and magnetism differ significantly from those of copper oxides. Experimental results demonstrate that $\text{La}_3\text{Ni}_2\text{O}_7$ undergoes a structural phase transition at approximately 12 GPa. Combined with thermodynamic enthalpy calculations of different structures, it has been determined that the space group of $\text{La}_3\text{Ni}_2\text{O}_7$ transitions from the low-pressure orthorhombic $Amam$ phase to the high-pressure $Fmmm$ phase[13, 14]. The Ni-apical oxygen atomic distance decreases from 2.297 Å in the ambient $Amam$ phase to 2.122 Å in the $Fmmm$ structure at 32.5 GPa. Additionally, the Ni-O-Ni angle between neighboring octahedra changes from 168° in the atmospheric pressure $Amam$ space group to 180° in the high-pressure $Fmmm$ space group[15, 5]. Recent theoretical studies employing various techniques, including DFT+U, DFT+DMFT, GW+DMFT, and model Hamiltonians, have investigated the

electronic structure of $\text{La}_3\text{Ni}_2\text{O}_7$ under pressure in relation to superconductivity. These studies emphasize the pivotal role of the Ni- d_{z^2} states near the Fermi level in superconductivity. The key degrees of freedom near the Fermi level are the two Ni- e_g orbitals, with the Ni- d_{z^2} orbital being nearly half-filled and the Ni- $d_{x^2-y^2}$ orbital being nearly quarter-filled.

The nickel-based superconductor $\text{La}_3\text{Ni}_2\text{O}_7$ has been the subject of several experimental and theoretical studies[5, 16, 17, 18, 19, 20, 21, 22, 23, 24, 25, 26, 27]. These investigations have explored various aspects of its electronic structure and superconducting properties. However, a systematic examination of the magnetic configurations in $\text{La}_3\text{Ni}_2\text{O}_7$ has not yet been conducted, leaving a gap in our understanding of this material’s magnetic behavior. In this work, we investigate the magnetic configurations in $\text{La}_3\text{Ni}_2\text{O}_7$ for both its low-pressure phase ($Amam$, space group No. 63) and high-pressure phase ($Fmmm$, space group No. 69). We examine the pressure-induced evolution of the magnetic ground state. Electronic structure calculations are performed for both phases, with emphasis on the orbitals near the Fermi level. Furthermore, we analyze phonon properties, including a detailed study of phonon vibration modes.

2. Methods

Our calculations consist of three main components. First, we optimize the lattice parameters of $\text{La}_3\text{Ni}_2\text{O}_7$ under various pressures using the Quantum ESPRESSO package[28]. The initial lattice parameters are: $Fmmm$ ($a = 5.289 \text{ \AA}$, $b = 5.218 \text{ \AA}$, $c = 19.734 \text{ \AA}$) and $Amam$ ($a = 5.439 \text{ \AA}$, $b = 5.376 \text{ \AA}$, $c = 20.403 \text{ \AA}$)[4, 29]. Second, we calculate the electronic structures incorporating correlation effects using density functional theory plus Hubbard U (DFT+ U)[30, 31] to account for local Coulomb interactions in Ni ($3d$). Third, we compute the phonon spectra and electron-phonon coupling of the $Amam$ and $Fmmm$ phases at different pressures using density functional perturbation theory, analyzed with PHONOPY package[32]. We set the charge density and wave function energy cutoffs to 60 Ry and 600 Ry, respectively. Perdew–Burke–Ernzerhof (PBE) generalized gradient approximation (GGA) pseudopotentials[33, 34] are employed, selected from the standard solid-state pseudopotentials (SSSP)[35, 36]. For the self-consistent field calculations, we use $16 \times 16 \times 16$ k -point grids and $8 \times 8 \times 8$ q -point grids.

3. Results and Discussion

To determine the ground state structure of $\text{La}_3\text{Ni}_2\text{O}_7$, we investigated two phases containing 8 Ni atoms, resulting in 70 possible antiferromagnetic (AFM) configurations. After excluding 35 configurations based on symmetry, we calculated the possible collinear spin order for the remaining 35 configurations. We also included calculations for the ferromagnetic (FM) configuration. Using experimentally known parameters to construct the crystal structure of $\text{La}_3\text{Ni}_2\text{O}_7$, we calculated the total energy for the non-magnetic (NM), FM, and 35 AFM configurations. As shown in Fig. 1(a)-(f), we focused primarily on three AFM structures of the $Fmmm$ and $Amam$ phases. In the G-AFM configuration, both intra- and interlayer couplings of the Ni layers exhibit AFM alignment. The C-AFM configuration displays intralayer AFM coupling and interlayer FM coupling in the Ni layers. Conversely, the A-AFM configuration exhibits intralayer FM coupling and interlayer AFM coupling in the Ni layers.

We investigate the pressure-dependent phase space within the DFT+ U framework, elucidating the magnetic behavior of $Fmmm$ and $Amam$ structures. The magnetic ground state calculations are performed with $U = 3.5$ eV and $J_H = 0.7$ eV. Our results indicate that the A-AFM phase constitutes the ground state for both $Fmmm$ and $Amam$ structures across the entire pressure range of 0-29.5 GPa. Table 1 lists the calculated total energies, crystal lattice parameters, and local magnetic moments for different possible magnetic configurations of $Fmmm$ and $Amam$ structures under various pressures. Before describing the pressure effect on the ground state of these structures, we briefly consider their ground states under ambient pressure. As shown in Table 1, without external pressure, the A-AFM configuration has the lowest total energy among all candidate configurations studied, suggesting it is the most stable magnetic structure. Notably, the energy differences between the various AFM (or FM) configurations and the NM configuration are exceptionally large in both $Fmmm$ and $Amam$ structures, indicating that the NM configuration is unlikely to be structurally stable. It should be noted that the lowest energy of A-AFM is determined from calculations of 35 antiferromagnetic configurations (See Appendix A of Supplementary materials).

We analyze the computational results of pressure-dependent calculations for key physical properties of the $Fmmm$ and $Amam$ structures. Specifically, we compute the total energies, crystal lattice parameters, and local magnetic

Table 1: Optimized lattice constants a , b , and c , relative enthalpies (E), and Ni magnetic moments (M_{Ni}) for $Fmmm$ and $Amam$ structures with various magnetic configurations at pressures from 0 to 29.5 GPa. Enthalpies are given relative to the $Amam$ -A-AFM phase and were calculated using DFT+ U ($U = 3.5$ eV, $J_H = 0.7$ eV). Complete enthalpy data for all 35 magnetic configurations are provided in Appendix A of the Supplementary Materials.

Structure	Pressure (GPa)	Phase	a (Å)	b (Å)	c (Å)	E (meV/atom)	M_{Ni} (μ_B)
$Fmmm$	0	A-AFM	5.381	5.356	20.034	22.16	1.16
		G-AFM	5.379	5.351	20.032	30.70	0.88
		C-AFM	5.380	5.351	20.032	34.03	1.00
		FM	5.376	5.352	20.042	35.49	1.27
		NM	5.390	5.359	20.064	55.70	0
	20	A-AFM	5.251	5.237	19.484	-27.50	1.10
		G-AFM	5.246	5.236	19.482	-22.30	0.79
		C-AFM	5.248	5.236	19.482	-17.92	0.91
		FM	5.249	5.237	19.486	-15.63	1.13
		NM	5.255	5.240	19.494	-3.96	0
	29.5	A-AFM	5.193	5.180	19.288	-33.91	1.06
		G-AFM	5.189	5.180	19.278	-29.95	0.68
		C-AFM	5.188	5.178	19.280	-25.58	0.87
		FM	5.192	5.180	19.288	-23.50	1.08
		NM	5.209	5.198	19.306	-11.83	0
$Amam$	0	A-AFM	5.395	5.419	20.085	0	1.21
		G-AFM	5.395	5.420	20.105	7.50	1.15
		C-AFM	5.398	5.422	20.121	12.08	1.07
		FM	5.395	5.418	20.098	12.91	1.31
		NM	5.435	5.516	20.141	47.50	0
	20	A-AFM	5.240	5.245	19.520	0	1.11
		G-AFM	5.241	5.247	19.521	6.66	0.84
		C-AFM	5.245	5.249	19.529	9.79	0.93
		FM	5.242	5.246	19.521	11.66	1.15
		NM	5.257	5.250	19.538	30.20	0
	29.5	A-AFM	5.207	5.181	19.308	0	1.09
		G-AFM	5.208	5.182	19.314	6.04	0.73
		C-AFM	5.210	5.185	19.309	8.33	0.90
		FM	5.208	5.183	19.314	11.48	1.10
		NM	5.219	5.218	19.360	21.87	0

moments for various possible magnetic configurations within a pressure range of 0-29.5 GPa. For simplicity, we select 0, 20, and 29.5 GPa as representative pressure points. As shown in Table 1, for all proposed states, as the pressure increases from 0 to 29.5 GPa, the A-AFM magnetic structure consistently presents the lowest energy, indicating it is the most stable magnetic configuration for both $Fmmm$ and $Amam$ structures within this pressure range. The optimized lattice parameters of the A-AFM phase for $Fmmm$ decrease with increasing pressure. At 0 GPa, they are $a = 5.381 \text{ \AA}$, $b = 5.356 \text{ \AA}$, and $c = 20.034 \text{ \AA}$, while at 29.5 GPa, they reduce to $a = 5.193 \text{ \AA}$, $b = 5.180 \text{ \AA}$, and $c = 19.288 \text{ \AA}$. Similarly, for the $Amam$ structure, the lattice parameters decrease from $a = 5.395 \text{ \AA}$, $b = 5.419 \text{ \AA}$, and $c = 20.085 \text{ \AA}$ at 0 GPa to $a = 5.207 \text{ \AA}$, $b = 5.181 \text{ \AA}$, and $c = 19.308 \text{ \AA}$ at 29.5 GPa. The calculated magnetic moments of different magnetic phases all decrease with increasing pressure, as shown in Table 1.

To further understand the electronic properties of the stable A-AFM configurations of $\text{La}_3\text{Ni}_2\text{O}_7$, we calculated the orbital-projected band structures, total density of states (TDOS), and orbital-resolved DOS of Ni 3d orbitals for $Fmmm$ and $Amam$ structures in the A-AFM phase at 29.5 GPa, as shown in Fig. 2(a) and (b). The Fermi level E_F is set to zero. In the orbital-projected electronic structures, the Ni $d_{x^2-y^2}$ orbital contribution is represented by brown lines, while Ni d_{xy} and Ni d_{z^2} are shown in red and dark green, respectively. For the $Fmmm$ structure, the TDOS at E_F is primarily composed of Ni d_{xy} and Ni d_{z^2} states. The Ni d_{xy} band crosses E_F , with its states mainly located between -2 eV and 2.5 eV. Ni $d_{x^2-y^2}$ states are concentrated between -3 eV and 0 eV, while Ni d_{z^2} states range from -2.4 eV to 2.5 eV. In the $Amam$ structure, Ni d_{xy} orbitals contribute significantly to the TDOS at E_F . The main difference from $Fmmm$ is that the maximum energy of the Ni d_{xy} band crossing E_F at the Γ point is shifted upward. Ni d_{xy} states are primarily located between -0.2 eV and 2.1 eV, Ni $d_{x^2-y^2}$ states between -3 eV and 0.5 eV, and Ni d_{z^2} states from -3 eV to 2.5 eV. Additionally, based on the crystal structure of $\text{La}_3\text{Ni}_2\text{O}_7$ -1313 at 300 K reported by Wang [37], we calculate the electronic structure of the non-magnetic state at 0 GPa (see Appendix B in Supplementary materials for band structure).

We calculated the phonon properties of $Fmmm$ and $Amam$ structures using primitive cells. The $Fmmm$ phase shows no imaginary modes at 12-29.5 GPa, indicating its dynamical stability in this pressure range. Figure 3 presents the phonon dispersion and phonon density of states (PHDOS) of $Fmmm$ at 29.5 GPa. The absence of imaginary vibrations in the entire

Brillouin zone confirms the structure's dynamical stability at this pressure. Phonon vibrations are mainly distributed in the middle and low frequencies. The PHDOS reveals that La atoms contribute most significantly to the density of states in the 100-200 cm^{-1} range, followed by Ni and O atoms. In the 200-550 cm^{-1} range, all atoms contribute, with O atoms showing the most pronounced effect, followed by Ni and La. A phonon energy gap appears in the 630-700 cm^{-1} range, where the PHDOS of all three atoms approaches zero. In the 700-900 cm^{-1} range, O atoms dominate the PHDOS, while La and Ni atoms contribute minimally. For the *Amam* phase, our calculations show stability at 0 GPa but imaginary modes at 15 GPa. Furthermore, using the $\text{La}_3\text{Ni}_2\text{O}_7$ -1313 crystal structure[37], we observe that the *Cmmm* phase exhibits imaginary modes in the pressure range of 20-30 GPa.

The primitive cell of *Fmmm* contains 12 atoms, resulting in 36 phonon bands: 3 acoustic and 33 optical branches. These can be irreducibly expressed as $4A_{1g} \oplus 6A_{2u} \oplus 14E_u \oplus 10E_g \oplus B_{2u} \oplus B_{1g}$. A_{2u} and E_u are infrared-active modes, while A_{1g} , B_{1g} , and E_g are Raman-active modes. Figure 4(a)-(d) shows the atomic vibrations of selected Raman and infrared modes: $A_{1g} \sim 490.7 \text{ cm}^{-1}$, $A_{2u} \sim 613.5 \text{ cm}^{-1}$, $A_{1g} \sim 629.4 \text{ cm}^{-1}$, and $A_{2u} \sim 709.7 \text{ cm}^{-1}$, respectively. At these frequencies, oxygen atoms dominate the vibrations. Combining the visualization of atomic vibrations with the PHDOS and analysis of Raman and infrared modes, we conclude that O atoms vibrate at higher frequencies than Ni and La atoms. This is primarily due to the significantly lower mass of O compared to Ni and La atoms.

In our study of the phonon properties of the *Fmmm* structure, we calculate the electron-phonon coupling and present the integration of the Eliashberg function $\alpha^2F(\omega)$ and electron-phonon coupling $\lambda(\omega)$ in the rightmost panel of Fig. 3. By integrating $\alpha^2F(\omega)$, we obtain $\lambda = 2 \int \alpha^2F(\omega)\omega^{-1}d\omega$ and the logarithmic average phonon frequency $\omega_{\text{ln}} = \exp[2\lambda^{-1} \int d\omega\alpha^2F(\omega)\omega^{-1} \log \omega]$. Our calculations show that λ remains small across all pressures studied. The λ_{e-ph} values for the three pressure points we calculated are 0.1326, 0.1870, and 0.1311, respectively. These results indicate that $\text{La}_3\text{Ni}_2\text{O}_7$ is not an electron-phonon-dominated superconductor and suggests it may be an unconventional superconductor that deviates from standard BCS theory.

4. Conclusion

In this study, we have conducted a comprehensive investigation of the magnetic, electronic, and phonon properties of $\text{La}_3\text{Ni}_2\text{O}_7$ across the pressure

range from 0 to 29.5 GPa. Our key findings include the determination of 35 antiferromagnetic configurations, with the A-AFM phase being identified as the ground state in the pressure range of 0-29.5 GPa. Analysis of the electronic structure of the ground state magnetic configuration reveals that the energy near the Fermi level E_F is primarily contributed by the d orbitals of Ni atoms, particularly the Ni d_{xy} and Ni d_{z^2} orbitals. Furthermore, the phonon dispersions for the $Fmmm$ phase of $\text{La}_3\text{Ni}_2\text{O}_7$ show no imaginary modes from 12 to 29.5 GPa, indicating dynamical stability in this pressure range, while the $Amam$ phase is found to be dynamically stable at 0 GPa. Notably, the calculated electron-phonon coupling constant λ_{e-ph} is small across all pressures studied, suggesting that if $\text{La}_3\text{Ni}_2\text{O}_7$ exhibits superconductivity, it may involve mechanisms beyond the conventional BCS theory.

5. Acknowledgments

This work is supported by the National Natural Science Foundation of China (Grants No. 12374135, 12175107), Natural Science Foundation of Nanjing University of Posts and Telecommunications (Grants No. NY224165, NY219087, NY220038) and the Hua Li Talents Program of Nanjing University of Posts and Telecommunications. Some of the calculations were performed on the supercomputer in the Big Data Computing Center (BDCC) of Southeast University.

Appendix A. Supplementary data

See the supplementary material for the energy differences in various magnetic configurations, band structures, and phonon spectra of $\text{La}_3\text{Ni}_2\text{O}_7$ under pressures.

References

- [1] M. Daghofer, A. Nicholson, A. Moreo, E. Dagotto, Three orbital model for the iron-based superconductors, *Phys. Rev. B* 81 (2010) 014511, <https://link.aps.org/doi/10.1103/PhysRevB.81.014511>.
- [2] D. Li, K. Lee, B. Y. Wang, M. Osada, S. Crossley, H. R. Lee, Y. Cui, Y. Hikita, H. Y. Hwang, Superconductivity in an infinite-layer nickelate,

- Nature 572 (7771) (2019) 624–627, <https://doi.org/10.1038/s41586-019-1496-5>.
- [3] M. Osada, B. Y. Wang, B. H. Goodge, K. Lee, H. Yoon, K. Sakuma, D. Li, M. Miura, L. F. Kourkoutis, H. Y. Hwang, A superconducting praseodymium nickelate with infinite layer structure, *Nano Letters* 20 (8) (2020) 5735–5740, <https://doi.org/10.1021/acs.nanolett.0c01392>.
- [4] H. Sun, M. Huo, X. Hu, J. Li, Z. Liu, Y. Han, L. Tang, Z. Mao, P. Yang, B. Wang, J. Cheng, D.-X. Yao, G.-M. Zhang, M. Wang, Signatures of superconductivity near 80 K in a nickelate under high pressure, *Nature* 621 (7979) (2023) 493–498, <https://doi.org/10.1038/s41586-023-06408-7>.
- [5] J. Hou, P.-T. Yang, Z.-Y. Liu, J.-Y. Li, P.-F. Shan, L. Ma, G. Wang, N.-N. Wang, H.-Z. Guo, J.-P. Sun, Y. Uwatoko, M. Wang, G.-M. Zhang, B.-S. Wang, J.-G. Cheng, Emergence of high-temperature superconducting phase in pressurized $\text{La}_3\text{Ni}_2\text{O}_7$ crystals, *Chinese Physics Letters* 40 (11) (2023) 117302, <https://dx.doi.org/10.1088/0256-307X/40/11/117302>.
- [6] Q.-G. Yang, D. Wang, Q.-H. Wang, Possible s_{\pm} -wave superconductivity in $\text{La}_3\text{Ni}_2\text{O}_7$, *Phys. Rev. B* 108 (2023) L140505, <https://doi.org/10.1103/PhysRevB.108.L140505>.
- [7] M. Azuma, Z. Hiroi, M. Takano, Y. Bando, Y. Takeda, Superconductivity at 110 K in the infinite-layer compound $(\text{Sr}_{1-x}\text{Ca}_x)_{1-y}\text{CuO}_2$, *Nature* 356 (6372) (1992) 775–776, <http://dx.doi.org/10.1038/356775a0>.
- [8] L. Azzouz, M. Halit, M. Rérat, R. Khenata, A. K. Singh, M. Obeid, H. R. Jappor, X. Wang, Structural, electronic and optical properties of ABTe_2 ($A = \text{Li, Na, K, Rb, Cs}$ and $B = \text{Sc, Y, La}$): Insights from first-principles computations, *Journal of Solid State Chemistry* 279 (2019) 120954, <https://doi.org/10.1016/j.jssc.2019.120954>.
- [9] M. M. Obeid, H. R. Jappor, S. J. Edrees, M. M. Shukur, R. Khenata, Y. Mogulkoc, The electronic, half-metallic, and magnetic properties of $\text{Ca}_{1-x}\text{Cr}_x\text{S}$ ternary alloys: Insights from the first-principle calculations, *Journal of Molecular Graphics and Modelling* 89 (2019) 22–32, <https://doi.org/10.1016/j.jmkgm.2019.02.004>.

- [10] H. Sakakibara, H. Usui, K. Suzuki, T. Kotani, H. Aoki, K. Kuroki, Model construction and a possibility of cupratelike pairing in a new d^9 nickelate superconductor $(Nd,Sr)NiO_2$, Phys. Rev. Lett. 125 (2020) 077003, <https://doi.org/10.1103/PhysRevLett.125.077003>.
- [11] M. Jiang, M. Berciu, G. A. Sawatzky, Critical nature of the ni spin state in doped $NdNiO_2$, Phys. Rev. Lett. 124 (2020) 207004, <https://doi.org/10.1103/PhysRevLett.124.207004>.
- [12] P. Werner, S. Hoshino, Nickelate superconductors: Multiorbital nature and spin freezing, Phys. Rev. B 101 (2020) 041104, <https://doi.org/10.1103/PhysRevB.101.041104>.
- [13] V. Voronin, I. Berger, V. Cherepanov, L. Gavrilova, A. Petrov, A. Ancharov, B. Tolochko, S. Nikitenko, Neutron diffraction, synchrotron radiation and exafs spectroscopy study of crystal structure peculiarities of the lanthanum nickelates $La_{n+1}Ni_nO_y$ ($n=1,2,3$), Nuclear Instruments and Methods in Physics Research Section A: Accelerators, Spectrometers, Detectors and Associated Equipment 470 (1) (2001) 202–209, [https://doi.org/10.1016/S0168-9002\(01\)01036-1](https://doi.org/10.1016/S0168-9002(01)01036-1).
- [14] Z. Liu, H. Sun, M. Huo, X. Ma, Y. Ji, E. Yi, L. Li, H. Liu, J. Yu, Z. Zhang, Z. Chen, F. Liang, H. Dong, H. Guo, D. Zhong, B. Shen, S. Li, M. Wang, Evidence for charge and spin density waves in single crystals of $La_3Ni_2O_7$ and $La_3Ni_2O_6$, Science China Physics, Mechanics & Astronomy 66 (1) (2022) 217411, <https://doi.org/10.1007/s11433-022-1962-4>.
- [15] Q. Qin, Y.-f. Yang, High- T_c superconductivity by mobilizing local spin singlets and possible route to higher T_c in pressurized $La_3Ni_2O_7$, Phys. Rev. B 108 (2023) L140504, <https://doi.org/10.1103/PhysRevB.108.L140504>.
- [16] A. Kushwaha, S. Mishra, M. Vishwakarma, S. Chauhan, H. R. Jappor, R. Khenata, S. Bin Omran, Theoretical study of thermal conductivity, mechanical, vibrational and thermodynamical properties of $Ln_2Zr_2O_7$ ($Ln = La, Nd, Sm, \text{ and } Eu$) pyrochlore, Inorganic Chemistry Communications 127 (2021) 108495, <https://doi.org/10.1016/j.inoche.2021.108495>.

- [17] A. Bafekry, I. Abdolhosseini Sarsari, M. Faraji, M. M. Fadlallah, H. R. Jappor, S. Karbasizadeh, V. Nguyen, M. Ghergherehchi, Electronic and magnetic properties of two-dimensional of FeX (X = S, Se, Te) monolayers crystallize in the orthorhombic structures, *Applied Physics Letters* 118 (14) (2021) 143102, <https://doi.org/10.1063/5.0046721>.
- [18] Y.-B. Liu, J.-W. Mei, F. Ye, W.-Q. Chen, F. Yang, s^\pm -wave pairing and the destructive role of apical-oxygen deficiencies in $\text{La}_3\text{Ni}_2\text{O}_7$ under pressure, *Phys. Rev. Lett.* 131 (2023) 236002, <https://doi.org/10.1103/PhysRevLett.131.236002>.
- [19] Z. Liao, L. Chen, G. Duan, Y. Wang, C. Liu, R. Yu, Q. Si, Electron correlations and superconductivity in $\text{La}_3\text{Ni}_2\text{O}_7$ under pressure tuning, *Phys. Rev. B* 108 (2023) 214522, <https://doi.org/10.1103/PhysRevB.108.214522>.
- [20] E. F. Talantsev, V. V. Chistyakov, Debye temperature, electron-phonon coupling constant, and microcrystalline strain in highly-compressed $\text{La}_3\text{Ni}_2\text{O}_{7-\delta}$, arXiv preprint arXiv:2401.00804 (2024), <https://doi.org/10.48550/arXiv.2401.00804>.
- [21] L. Craco, S. Leoni, Strange metal and coherence-incoherence crossover in pressurized $\text{La}_3\text{Ni}_2\text{O}_7$, *Phys. Rev. B* 109 (2024) 165116, <https://doi.org/10.1103/PhysRevB.109.165116>.
- [22] T. Kaneko, H. Sakakibara, M. Ochi, K. Kuroki, Pair correlations in the two-orbital hubbard ladder: Implications for superconductivity in the bilayer nickelate $\text{La}_3\text{Ni}_2\text{O}_7$, *Phys. Rev. B* 109 (2024) 045154, <https://doi.org/10.1103/PhysRevB.109.045154>.
- [23] Y. Zhang, L.-F. Lin, A. Moreo, T. A. Maier, E. Dagotto, Electronic structure, magnetic correlations, and superconducting pairing in the reduced ruddlesden-popper bilayer $\text{La}_3\text{Ni}_2\text{O}_6$ under pressure: Different role of $d_{3z^2-r^2}$ orbital compared with $\text{La}_3\text{Ni}_2\text{O}_7$, *Phys. Rev. B* 109 (2024) 045151, <https://doi.org/10.1103/PhysRevB.109.045151>.
- [24] C. Lu, Z. Pan, F. Yang, C. Wu, Interlayer-coupling-driven high-temperature superconductivity in $\text{La}_3\text{Ni}_2\text{O}_7$ under pressure, *Phys. Rev. Lett.* 132 (2024) 146002, <https://doi.org/10.1103/PhysRevLett.132.146002>.

- [25] R. Jiang, J. Hou, Z. Fan, Z.-J. Lang, W. Ku, Pressure driven fractionalization of ionic spins results in cupratelike high- T_c superconductivity in $\text{La}_3\text{Ni}_2\text{O}_7$, *Phys. Rev. Lett.* 132 (2024) 126503, <https://doi.org/10.1103/PhysRevLett.132.126503>.
- [26] L. C. Rhodes, P. Wahl, Structural routes to stabilize superconducting $\text{La}_3\text{Ni}_2\text{O}_7$ at ambient pressure, *Phys. Rev. Mater.* 8 (2024) 044801, <https://doi.org/10.1103/PhysRevMaterials.8.044801>.
- [27] J. Yang, H. Sun, X. Hu, Y. Xie, T. Miao, H. Luo, H. Chen, B. Liang, W. Zhu, G. Qu, C.-Q. Chen, M. Huo, Y. Huang, S. Zhang, F. Zhang, F. Yang, Z. Wang, Q. Peng, H. Mao, G. Liu, Z. Xu, T. Qian, D.-X. Yao, M. Wang, L. Zhao, X. J. Zhou, Orbital-dependent electron correlation in double-layer nickelate $\text{La}_3\text{Ni}_2\text{O}_7$, *Nature Communications* 15 (1) (2024) 4373, <https://doi.org/10.1038/s41467-024-48701-7>.
- [28] P. Giannozzi, S. Baroni, N. Bonini, M. Calandra, R. Car, C. Cavazzoni, D. Ceresoli, G. L. Chiarotti, M. Cococcioni, I. Dabo, A. D. Corso, S. de Gironcoli, S. Fabris, G. Fratesi, R. Gebauer, U. Gerstmann, C. Gougoussis, A. Kokalj, M. Lazzeri, L. Martin-Samos, N. Marzari, F. Mauri, R. Mazzarello, S. Paolini, A. Pasquarello, L. Paulatto, C. Sbraccia, S. Scandolo, G. Sclauzero, A. P. Seitsonen, A. Smogunov, P. Umari, R. M. Wentzcovitch, Quantum espresso: a modular and open-source software project for quantum simulations of materials, *Journal of Physics: Condensed Matter* 21 (39) (2009) 395502, <https://dx.doi.org/10.1088/0953-8984/21/39/395502>.
- [29] Z. Luo, X. Hu, M. Wang, W. Wú, D.-X. Yao, Bilayer two-orbital model of $\text{La}_3\text{Ni}_2\text{O}_7$ under pressure, *Phys. Rev. Lett.* 131 (2023) 126001, <https://doi.org/10.1103/PhysRevLett.131.126001>.
- [30] D. S. Lambert, D. D. O'Regan, Use of $DFT + U + J$ with linear response parameters to predict non-magnetic oxide band gaps with hybrid-functional accuracy, *Phys. Rev. Res.* 5 (2023) 013160, <https://doi.org/10.1103/PhysRevResearch.5.013160>.
- [31] M. Yu, S. Yang, C. Wu, N. Marom, Machine learning the hubbard U parameter in $DFT+U$ using bayesian optimization, *npj Computational Materials* 6 (1) (2020) 180, <https://doi.org/10.1038/s41524-020-00446-9>.

- [32] A. Togo, I. Tanaka, First principles phonon calculations in materials science, *Scripta Materialia* 108 (2015) 1–5, <https://doi.org/10.1016/j.scriptamat.2015.07.021>.
- [33] J. P. Perdew, K. Burke, M. Ernzerhof, Generalized gradient approximation made simple, *Phys. Rev. Lett.* 77 (1996) 3865–3868, <https://doi.org/10.1103/PhysRevLett.77.3865>.
- [34] G. Kresse, D. Joubert, From ultrasoft pseudopotentials to the projector augmented-wave method, *Phys. Rev. B* 59 (1999) 1758–1775, <https://doi.org/10.1103/PhysRevB.59.1758>.
- [35] K. Lejaeghere, G. Bihlmayer, T. Björkman, P. Blaha, S. Blügel, V. Blum, D. Caliste, I. E. Castelli, S. J. Clark, A. D. Corso, S. de Gironcoli, T. Deutsch, J. K. Dewhurst, I. D. Marco, C. Draxl, M. Dułak, O. Eriksson, J. A. Flores-Livas, K. F. Garrity, L. Genovese, P. Gianozzi, M. Giantomassi, S. Goedecker, X. Gonze, O. Grånäs, E. K. U. Gross, A. Gulans, F. Gygi, D. R. Hamann, P. J. Hasnip, N. A. W. Holzwarth, D. Iuşan, D. B. Jochym, F. Jollet, D. Jones, G. Kresse, K. Koepnik, E. Küçükbenli, Y. O. Kvashnin, I. L. M. Locht, S. Lubeck, M. Marsman, N. Marzari, U. Nitzsche, L. Nordström, T. Ozaki, L. Paulatto, C. J. Pickard, W. Poelmans, M. I. J. Probert, K. Refson, M. Richter, G.-M. Rignanese, S. Saha, M. Scheffler, M. Schlipf, K. Schwarz, S. Sharma, F. Tavazza, P. Thunström, A. Tkatchenko, M. Torrent, D. Vanderbilt, M. J. van Setten, V. V. Speybroeck, J. M. Wills, J. R. Yates, G.-X. Zhang, S. Cottenier, Reproducibility in density functional theory calculations of solids, *Science* 351 (6280) (2016) aad3000, <https://doi.org/10.1126/science.aad3000>.
- [36] G. Prandini, A. Marrazzo, I. E. Castelli, N. Mounet, N. Marzari, Precision and efficiency in solid-state pseudopotential calculations, *npj Computational Materials* 4 (1) (2018) 72, <https://doi.org/10.1038/s41524-018-0127-2>.
- [37] H. Wang, L. Chen, A. Rutherford, H. Zhou, W. Xie, Long-range structural order in a hidden phase of ruddlesden–popper bilayer nickelate $\text{La}_3\text{Ni}_2\text{O}_7$, *Inorganic Chemistry* 63 (11) (2024) 5020–5026, <https://doi.org/10.1021/acs.inorgchem.3c04474>.

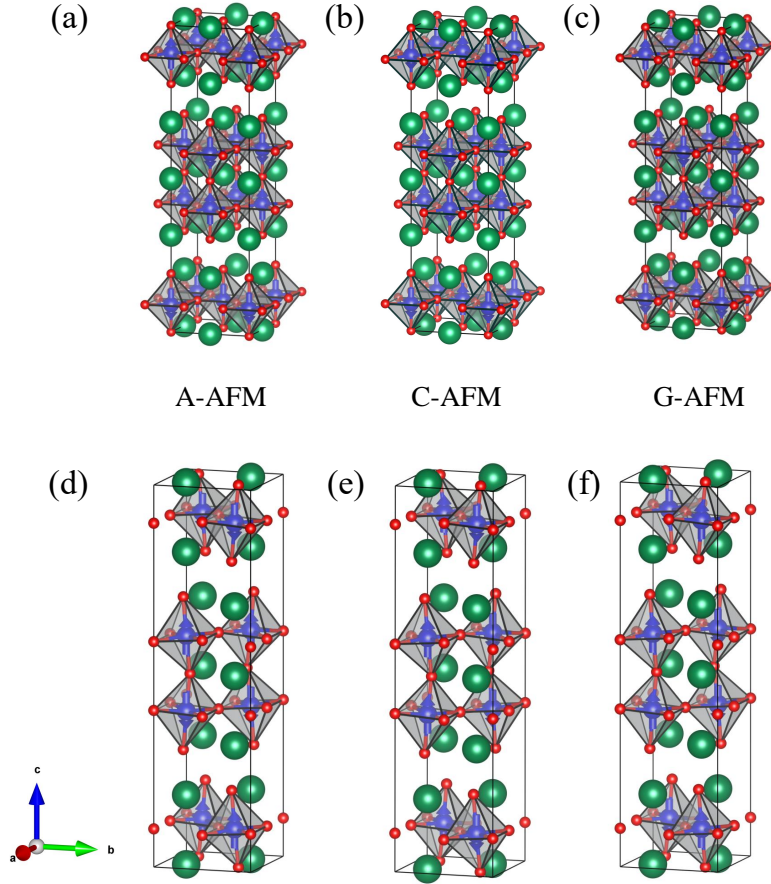


Figure 1: The geometrical structural models of $\text{La}_3\text{Ni}_2\text{O}_7$ with different magnetic configurations. (a)-(c) represent the $Fm\bar{3}m$ structure, corresponding to the A-AFM, C-AFM, and G-AFM phases, respectively. (d)-(f) represent the $Amam$ structure, corresponding to the A-AFM, C-AFM, and G-AFM phases, respectively. Green, blue, and red spheres indicate La, Ni, and O atoms, respectively. Blue arrows on the Ni atoms indicate the directions of magnetic moments.

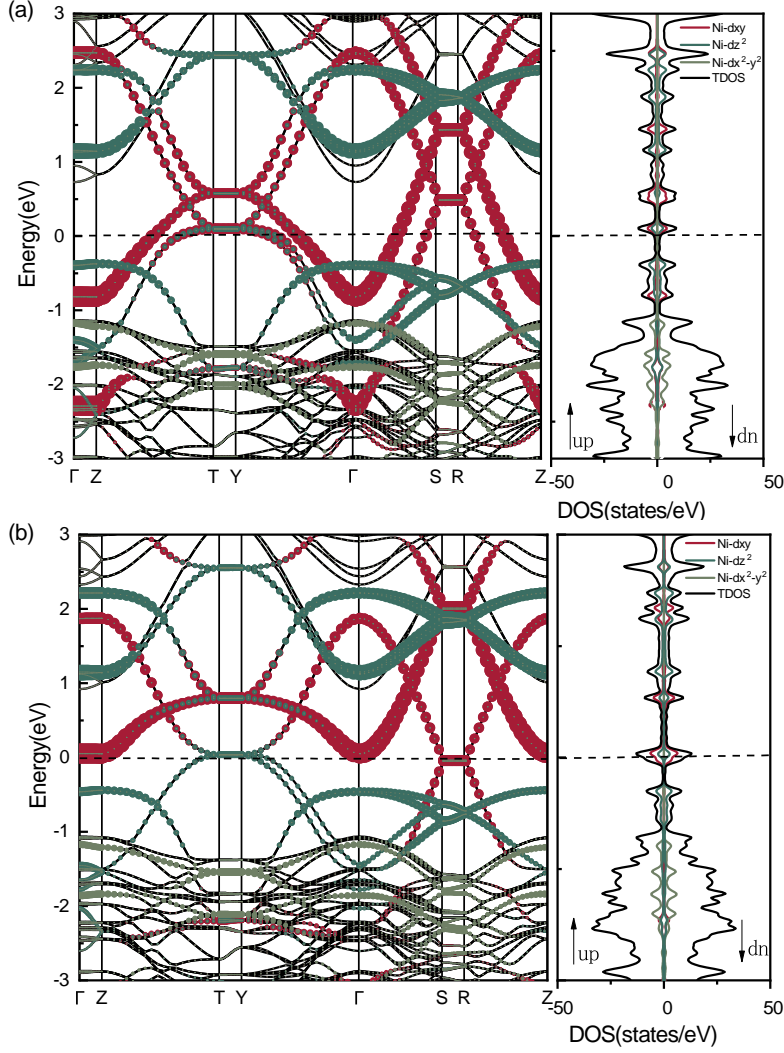


Figure 2: Electronic band structures (left panels) and total and Ni d -resolved density of states (right panels) for spin-up (down) in the A-AFM configuration of (a) $Fmmm$ and (b) $Amam$ structures under 29.5 GPa. The Fermi level E_F is set to zero. Ni d_{xy} (Ni d_{z^2}) is shown in red (dark green), and Ni $d_{x^2-y^2}$ is shown in brown. Band structures for the remaining pressure points are shown in Appendix B of Supplementary materials.

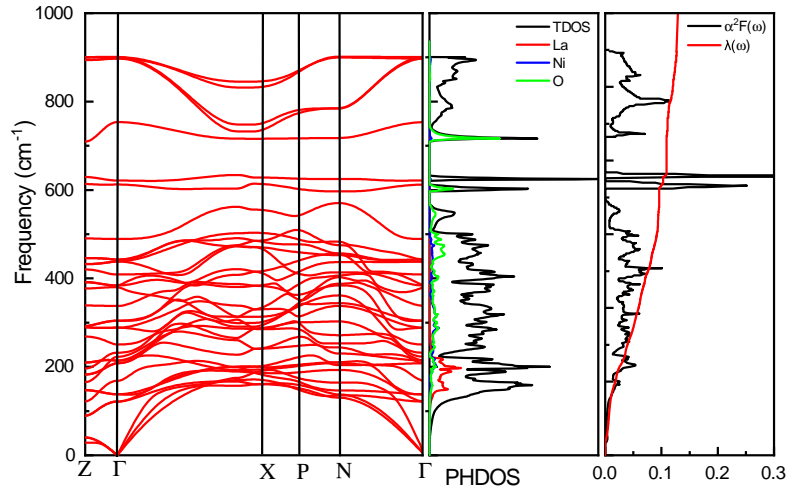


Figure 3: Left panel: phonon dispersion. Middle panel: phonon density of states. Right panel: Eliashberg spectral function $\alpha^2F(\omega)$ and electron-phonon coupling $\lambda(\omega)$ of the $Fmmm$ structure at 29.5 GPa. The PHDOS projections on La, Ni, and O are color-coded in red, blue, and green, respectively. Results for other pressure points are shown in Appendix C of Supplementary materials.

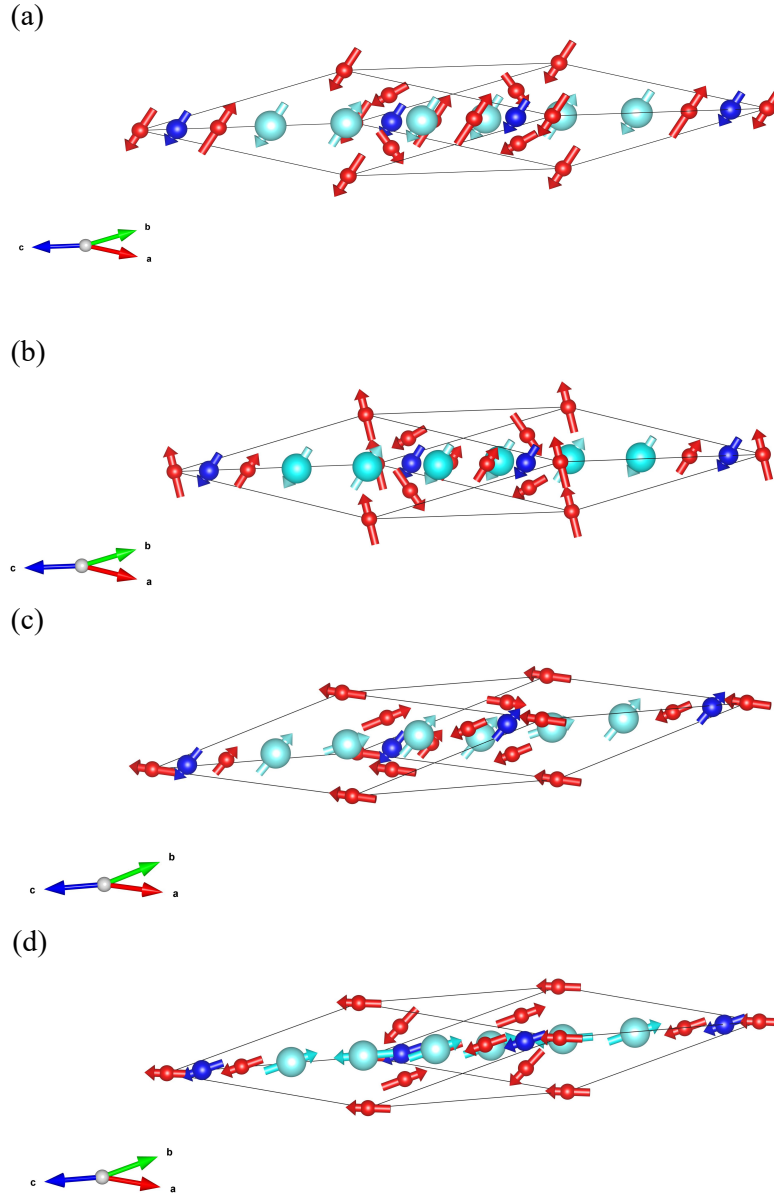


Figure 4: Visualization of atomic vibrations for selected phonon modes in $\text{La}_3\text{Ni}_2\text{O}_7$: (a) $A_{1g} \sim 490.7 \text{ cm}^{-1}$, (b) $A_{2u} \sim 613.5 \text{ cm}^{-1}$, (c) $A_{1g} \sim 629.4 \text{ cm}^{-1}$, and (d) $A_{2u} \sim 709.7 \text{ cm}^{-1}$. Red, cyan, and blue spheres represent O, La, and Ni atoms, respectively. Arrows indicate vibration directions, with arrow length proportional to vibration amplitude.